



## The Low Temperature Corona in ESO 511–G030 Revealed by *NuSTAR* and *XMM-Newton*

ZUOBIN ZHANG,<sup>1</sup> JIACHEN JIANG <sup>2</sup>, HONGHUI LIU,<sup>1</sup> COSIMO BAMBI <sup>1</sup>, CHRISTOPHER S. REYNOLDS,<sup>2</sup>  
ANDREW C. FABIAN,<sup>2</sup> THOMAS DAUSER,<sup>3</sup> KRISTIN MADSEN,<sup>4,5</sup> ANDREW YOUNG,<sup>6</sup> LUIGI GALLO,<sup>7</sup> ZHIBO YU,<sup>1</sup> AND  
JOHN TOMSICK<sup>8</sup>

<sup>1</sup>Center for Field Theory and Particle Physics and Department of Physics, Fudan University, 2005 Songhu Road, 200438 Shanghai, China

<sup>2</sup>Institute of Astronomy, University of Cambridge, Madingley Road, Cambridge CB3 0HA, UK

<sup>3</sup>Remeis-Observatory & ECAP, FAU Erlangen-Nürnberg, Sternwartstr. 7, 96049 Bamberg, Germany

<sup>4</sup>Cahill Center for Astronomy and Astrophysics, California Institute of Technology, Pasadena, CA 91125, USA

<sup>5</sup>CRESST and X-ray Astrophysics Laboratory, NASA Goddard Space Flight Center, Greenbelt, MD 20771 USA

<sup>6</sup>School of Physics, Tyndall Avenue, University of Bristol, Bristol BS8 1TH, UK

<sup>7</sup>Department of Astronomy and Physics, Saint Mary's University, 923 Robie Street, Halifax, NS B3H 3C 3, Canada

<sup>8</sup>Space Sciences Laboratory, University of California, 7 Gauss Way, Berkeley, CA 94720-7450, USA

### ABSTRACT

We present the results from a coordinated *XMM-Newton* + *NuSTAR* observation of the Seyfert 1 Galaxy ESO 511–G030. With this joint monitoring programme, we conduct a detailed variability and spectral analysis. The source remained in a low flux and very stable state throughout the observation period, although there are slight fluctuations of flux over long timescales. The broadband (0.3–78 keV) spectrum shows the presence of a power-law continuum with a soft excess below 2 keV, a relatively narrow iron K $\alpha$  emission ( $\sim 6.4$  keV), and an obvious cutoff at high energies. We find that the soft excess can be modeled by two different possible scenarios: a warm ( $kT_e \sim 0.19$  keV) and optically thick ( $\tau \sim 18 \sim 25$ ) Comptonizing corona or a relativistic reflection from a high-density ( $\log[n_e/\text{cm}^{-3}] = 17.1 \sim 18.5$ ) inner disc. All models require a low temperature ( $kT_e \sim 13$  keV) for the hot corona.

*Keywords:* accretion, accretion discs – black hole physics – galaxies: Seyfert – X-rays: galaxies.

### 1. INTRODUCTION

Active galactic nuclei (AGNs) are luminous sources in the Universe over a broad energy range from radio to gamma rays. This emission results from the accretion of matter onto a supermassive black hole (SMBH) at the center of its host galaxy (Lynden-Bell 1969; Rees 1984). By studying the X-ray emission, we can directly probe the innermost region of AGNs. The AGN X-ray emission region is small in size (Reis & Miller 2013) and located close to the central SMBH and accretion disc, as suggested by studies of black hole mass dependence of AGN X-ray variability (e.g., Axelsson et al. 2013; McHardy 2013; Ludlam et al. 2015), reverberation of X-ray radiation reprocessed by the accretion disc (e.g., De Marco et al. 2013; Uttley et al. 2014; Kara et al.

2016), and quasar microlensing (e.g., Mosquera et al. 2013; Chartas et al. 2016; Guerras et al. 2017).

The typical broadband X-ray spectrum of a Seyfert 1 AGN consists of a power-law continuum, fluorescent emission lines, a Compton hump, and a soft excess below  $\sim 2$  keV. In the simplest scenario, thermal emission from the disc mostly emits in the ultraviolet (UV) band. The seed UV/optical photons are Compton up-scattered to the hard X-ray band in a region filled with a hot and optically thin plasma near the central black hole, which is often referred to as the corona (e.g., Vaiana & Rosner 1978; Haardt & Maraschi 1991; Merloni & Fabian 2003). A fraction of the hard X-ray photons illuminate the surface of the accretion disc and are reflected to produce the reflection component (e.g., Ross & Fabian 2005; García & Kallman 2010, which is smeared by relativistic effects (e.g., Bambi et al. 2021; Fabian et al. 1989).

Broadband X-ray spectroscopy of the X-ray emission produced in the Comptonizing plasma can provide important insights into the principal properties of the

corona, such as its temperature ( $kT_e$ ), optical depth ( $\tau_e$ ), and ultimately its geometry. The continuum originates in the Comptonization processes of low-energy disc photons scattered by hot electrons (e.g., Baloković et al. 2020). The high-energy turnover is generally interpreted as the temperature of the corona (or a value close to it). Recently, Fabian et al. (2015) gathered results from *NuSTAR* to map out their locations on the compactness-temperature ( $\ell - \Theta$ ) diagram, and found many sources are (marginally) above the electron–electron coupling line and all are above the electron–proton line. Then Fabian et al. (2017) re-examined the case of hybrid coronae (Zdziarski et al. 1993), where the plasma contains both thermal and non-thermal particles, and found that objects with the lowest coronal temperature measurements require the largest non-thermal fractions.

ESO 511–G030 is a bare Seyfert 1 AGN at redshift  $z = 0.0224$  (Tombesi et al. 2010, Winter et al. 2012, and Laha et al. 2014). It is found to be one of the brightest bare Seyfert AGNs featured in the Swift 58 month BAT catalog (Winter et al. 2012). Ghosh & Laha (2021) presented a broadband (optical-UV to hard X-ray) spectral study of ESO 511–G030 using multi-epoch *Suzaku* and *XMM-Newton* (Jansen et al. 2001) data from 2007 and 2012. They investigated the spectral features observed in the source with a physically motivated set of models and reported a rapidly spinning black hole ( $a_* > 0.78$ ) and a compact corona, indicating a relativistic origin of the broad Fe emission line. Ghosh & Laha (2021) also found an inner disc temperature of  $2 \sim 3$  eV, which characterizes the UV bump, and that the SMBH accretes at a sub-Eddington rate ( $\lambda_{\text{Edd}} = 0.004 - 0.008$ ).

Previous studies of ESO 511–G030 were based on the *XMM-Newton* observation data in 2007 and the *Suzaku* observation in 2012 (e.g., Ghosh & Laha 2021, Tombesi et al. 2010, Winter et al. 2012, and Laha et al. 2014). *NuSTAR* (Harrison et al. 2013) and *XMM-Newton* conducted a joint observing campaign on this source in 2019, consisting of five joint observations over twenty days. In this paper, we analyze the observational data from this *NuSTAR* and *XMM-Newton* joint observation campaign, investigating the nature of the corona continuum, reflection, and soft excess.

The paper is organized as follows. In Sec. 2, we present the observational data reduction and the light curves. The spectral analysis with two different possible scenarios is reported in Sec. 3. We discuss the results and report our conclusions in Sec. 4 and Sec. 5, respectively.

## 2. OBSERVATIONS AND DATA REDUCTION

During the period of 07-20-2019 to 08-09-2019, *NuSTAR* and *XMM-Newton* performed five joint observa-

tions. The details of these observations are in Tab. 1. These data are taken with two focal plane modules, named FPMA and FPMB, on board the *NuSTAR* satellite, and EPIC-pn CCD modules, on board of *XMM-Newton*. A total unfiltered exposure time of  $\sim 168$  ks with five different observations is obtained.

### 2.1. *XMM-Newton* data reduction

The *XMM-Newton* EPIC cameras offer the possibility of performing extremely sensitive imaging observations over a field of view of  $30'$  and the energy range from 0.2 to 12 keV, with moderate spectral ( $E/\Delta E \sim 20 - 50$ ) and angular resolution ( $\sim 6''$  FWHM;  $\sim 15''$  HEW). Because of the higher effective area of EPIC-pn compared with EPIC-MOS and its consistency with EPIC-MOS data, we only consider EPIC-pn data in the 0.3–10.0 keV energy band in our X-ray spectral analysis.

We reduce the data and extract products from Observation Data Files (ODF) following the standard procedures based on the *XMM-Newton* Science Analysis System (SAS 18.0.0) and the latest calibration files. The EPIC-pn data are produced using `epproc` and processed with the standard filtering criterion. Then we remove periods of high background by creating a Good Time Interval (GTI) file using the task `tabgtigen`. The source products are extracted from a circular region with a radius of  $30''$  centered on the source, and the background is taken from a circular region with a radius of  $65''$  offset source. The `evselect` task was used to select single and double events for EPIC-pn (`PATTERN  $\leq$  4, FLAG == 0`) source event lists. The Redistribution Matrix File (RMF) and Ancillary Response File (ARF) are created by using the SAS tasks `rmfgen` and `arfgen`, respectively. We test the pile-up for these data by using the SAS task `epatplot` and find that the influence of pile-up events is negligible during the observations.

### 2.2. *NuSTAR* data reduction

The reduction of the *NuSTAR* (Harrison et al. 2013) data was conducted following the standard procedure using the *NuSTAR* Data Analysis Software (NUSTAR-DAS v.2.1.1), and updated calibration files from *NuSTAR* CALDB v20220301. We produce calibrated and filtered event files with `nupipeline`. Passages through the South Atlantic Anomaly are excluded from consideration using the following settings: `saamode = STRICT, SAACALC = 2` and `TENTACLE = YES`. For such an AGN source, the effect of the SAA filtering is non-negligible. To get more reliable spectra products, we use strict filtering criteria here to realize the reduction in the background rates.

We utilize the task package `nuproduct` to extract source products and their associated instrumental re-

**Table 1.** Summary of the observations analyzed in the present work.

	Mission	Obs. ID	Instrument	Start data	Exposure (ks)
Epoch 1	<i>NuSTAR</i>	60502035002	FPMA/B	2019-07-20	32.1
	<i>XMM-Newton</i>	0852010101	EPIC-pn	2019-07-20	37.0
Epoch 2	<i>NuSTAR</i>	60502035004	FPMA/B	2019-07-25	34.1
	<i>XMM-Newton</i>	0852010201	EPIC-pn	2019-07-25	36.0
Epoch 3	<i>NuSTAR</i>	60502035006	FPMA/B	2019-07-29	31.2
	<i>XMM-Newton</i>	0852010301	EPIC-pn	2019-07-29	33.0
Epoch 4	<i>NuSTAR</i>	60502035008	FPMA/B	2019-08-02	41.8
	<i>XMM-Newton</i>	0852010401	EPIC-pn	2019-08-02	38.3
Epoch 5	<i>NuSTAR</i>	60502035010	FPMA/B	2019-08-09	29.2
	<i>XMM-Newton</i>	0852010501	EPIC-pn	2019-08-09	36.2

sponse files from a circular region of radius  $65''$  centered on the source. The *NuSTAR* background varies across the field of view and between the four CdZnTe (CZT) detectors on each focal plane. For the background, we extract it from an optional maximal nearby polygon region free from source contamination, and we limit the background region on the CZT chip of the source, as shown in Fig. 1. With these strategies, we minimize the systematic errors from the instrument and obtain a more reliable background spectrum. The products are obtained from FPMA and FPMB separately.

### 2.3. Lightcurves and variability

Fig. 2 presents the light curves of *NuSTAR* and simultaneous *XMM-Newton* observations on Epoch 1-5. *XMM-Newton* data are binned in 150 s intervals and *NuSTAR* FPMA data and FPMB data are binned in 200 s intervals. The *XMM-Newton* 0.3 – 10 keV count rate of ESO 511–G030 remains consistent within the range of  $1.8 - 3.0 \text{ ct s}^{-1}$  during the first four epochs, and *NuSTAR* 3.0 – 78.0 keV count rate within the range of  $0.1 - 0.35 \text{ ct s}^{-1}$ . In Epoch 5, the light curve shows an increase of  $\sim 60\%$  both in *NuSTAR* and *XMM-Newton* count rates, compared to the average count rates of Epoch 1-4. In Epoch 5, which is the brightest epoch, the *XMM-Newton* light curve shows a count rate of  $\sim 3.5$  counts/s and *NuSTAR* shows a count rate of  $\sim 0.35$  counts/s. In Epoch 2, which is the faintest epoch, the *XMM-Newton* light curve shows a count rate of  $\sim 2.0$  counts/s and *NuSTAR* shows a count rate of  $\sim 0.2$  counts/s. Note that the photon rate fluctuation

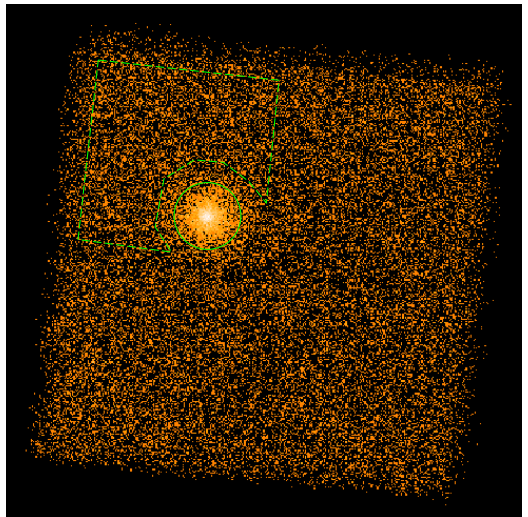


**Figure 1.** *NuSTAR* FPMB image of observation ID 60502035008 (ESO 511–G030). The source spectrum is extracted from the solid green circle region with a radius of  $65''$  and the background spectrum is extracted from the dashed green polygon.

between different observations occurs simultaneously in multiple instruments, indicating that the variability occurs simultaneously for the entire broad energy band.

To investigate this variability, we extract the *XMM-Newton* light curves in the 0.3–2.0 keV and 2–10 keV bands, shown in the upper panel of each plot in Fig. 3, which shows that both soft and hard energy bands vary simultaneously. Moreover, we plot the *XMM-Newton* hardness (2–10 keV/0.3–2.0 keV) ratio in the lower panel of each plot. The hardness presents a stable trend both

in a single observation and between observations. We also extract the spectra from divided epochs and only a tiny discrepancy in normalization is found between spectra, which confirms the result obtained from the light curve analysis.

As mentioned above, because variability occurs simultaneously for the entire broad energy band and the spectrum variations are only a discrepancy in normalization between the observations, we merge the spectra of Epoch 1-5 into a single spectrum. For *XMM-Newton*, we produce a combined multi-observation EPIC-pn spectrum using the SAS ftool `epicspeccombine` and we focus on the *XMM-Newton* data over the 0.3–10.0 keV band in the following analysis. For *NuSTAR*, we produce a combined multi-observation FPMA spectrum and FPMB spectrum using the HEASARC ftool `addspec` and we use the *NuSTAR* data over the 3.0–78.0 keV band. All spectra are rebinned to minimum counts of 20 per energy bin and oversample the spectral resolution by a factor of 3.

### 3. SPECTRAL ANALYSIS

In this section, we present an analysis of the time-averaged *NuSTAR* and *XMM-Newton* spectra using the XSPEC (v12.12.1) package (Arnaud 1996). To account for the differences between the detector responses of FPMA/B and EPIC-pn, we include a cross-calibration factor, which is fixed to unity for the EPIC-pn spectra, but varies freely for FPMA and FPMB (Madsen et al. 2015a). The  $\chi^2$  statistics is employed and all parameter uncertainties are estimated at 90% confidence level, corresponding to  $\Delta\chi^2 = 2.71$ . We include the absorption model `tbnew` to describe the Galactic absorption, using the recommended photoelectric cross sections of Verner et al. (1996). In addition, the multiplicative model `zmshift` is used to account for the redshift of the source and fix the redshift at  $z = 0.0224$  during the spectral fitting.

We start the fitting with an absorbed power-law model, i.e. `tbnew × powerlaw` in XSPEC language. `powerlaw` accounts for a power-law component from the corona. In this fit, we ignore the data below 3 keV, above 15 keV and the 5-7 keV band, i.e., we ignore the possible soft excess, the iron emission line, and Compton hump. Fig. 4 shows the broadband spectra of ESO 511–G030 (upper panel) and the extrapolated data-to-model ratios of the 0.3-78.0 keV dataset from the above fit. The typical AGN spectral features can be seen: a soft excess below 2 keV, Fe K $\alpha$  emission at  $\sim 6.4$  keV, a weak Compton hump peaking at  $\sim 20$  keV, and a cutoff at high energy.

**Table 2.** Summary of the models used in our analysis: blackbody, warm corona, and relativistic reflection.

Model	Component
1	<code>tbnew × zmshift × (bbody + nthcomp + xillverCp)</code>
2	<code>tbnew × zmshift × (nthcomp + nthcomp + xillverCp)</code>
3	<code>tbnew × zmshift × (relconv × xillverDCp + nthcomp + xillverCp)</code>

Fig. 5 presents a zoomed-in version of the residual in the 6 keV region. Both the *XMM-Newton* and *NuSTAR* spectra reveal a consistent shape for the iron K-shell emission line. To investigate the excess emission at 6~7 keV, we first introduce a `gaussian` model to the absorbed power-law model. The source frame line energy is consistent with 6.4 keV and line width  $\sigma = 0.04_{-0.03}^{+0.05}$  keV, which indicates the presence of a relatively narrow Fe emission line in ESO 511–G030. These features can be partially accounted for by a reprocessing of X-ray photons in a neutral and distant material, free from relativistic effects, possibly in the broad-line region (e.g., Costantini et al. 2016; Nardini et al. 2016), or the torus (e.g., Yaqoob et al. 2007; Marinucci et al. 2018). To probe the cutoff at high energies, we replace `powerlaw` with `nthcomp` (Zdziarski et al. 1996; Życki et al. 1999). This model reveals a low temperature corona,  $kT_e = 16_{-4}^{+5}$  keV. In our subsequent analysis, we will investigate it with more physical models.

To fit the soft excess, we separately try a phenomenological single temperature blackbody model, a warm corona model, and a high-density relativistic reflection model. The fits with these models are presented and discussed in the following subsections. The models are summarized in Tab. 2. The data-to-model ratios of the fits are depicted in the left column of Fig. 6 and the best-fit models are shown in Fig. 10. The best-fit results are summarized in Tab. 3, where  $\nu$  is the number of degrees of freedom (dof) and  $\chi_{\text{red}}^2 = \chi^2/\nu$  is the reduced  $\chi^2$ . Instead of the normalization of every component, in Tab. 3 we report the flux of every component calculated by `cflux` over the energy range 0.3-80.0 keV.

#### 3.1. Model 1: phenomenological blackbody model

In this fit, we use the single temperature blackbody model `bbody` to describe the soft excess. The coronal emission is described by `nthcomp` with the seed photons originating from the disc. In addition, we introduce `xillverCp` (García & Kallman 2010; García et al. 2011, 2013) to account for the reprocessed emission from the disc with reflection fraction  $F_{\text{ref}}$  fixed to  $-1$ . In XSPEC notation, the phenomenological model reads as `tbnew ×`



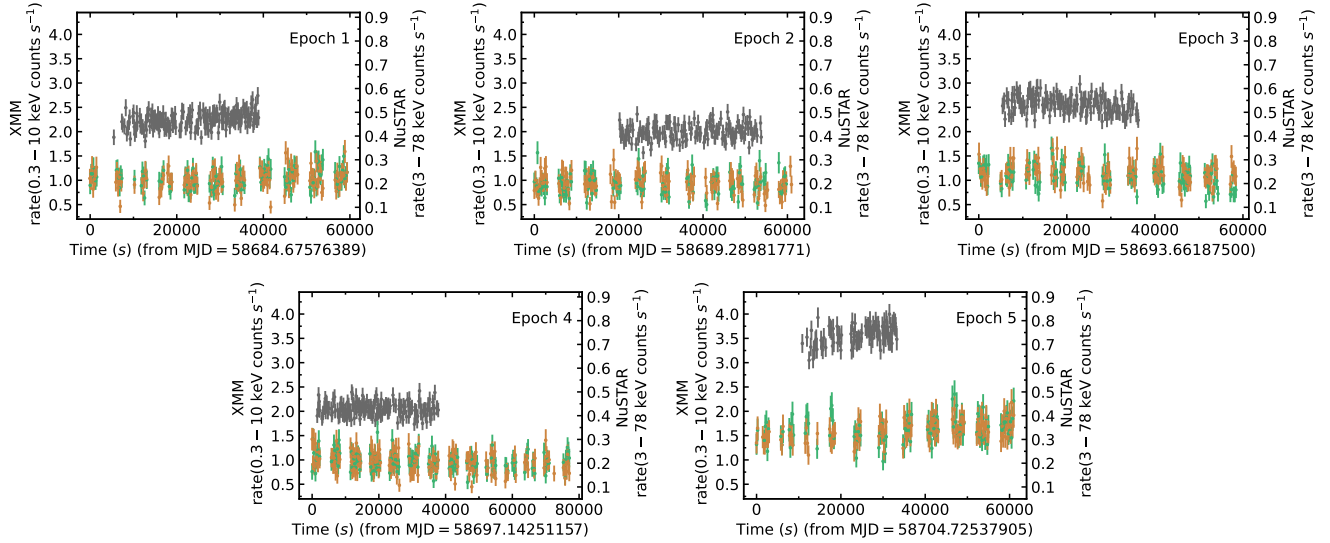


**Figure 2.** Light curves of *NuSTAR* and simultaneous *XMM-Newton* observations of ESO 511–G030. The *XMM-Newton* data are binned in 150 s intervals and shown in grey. The *NuSTAR* FPMA and FPMB data are binned in 200 s intervals and shown in orange and green, respectively. ESO 511–G030 remains in a consistent flux state during each observation.

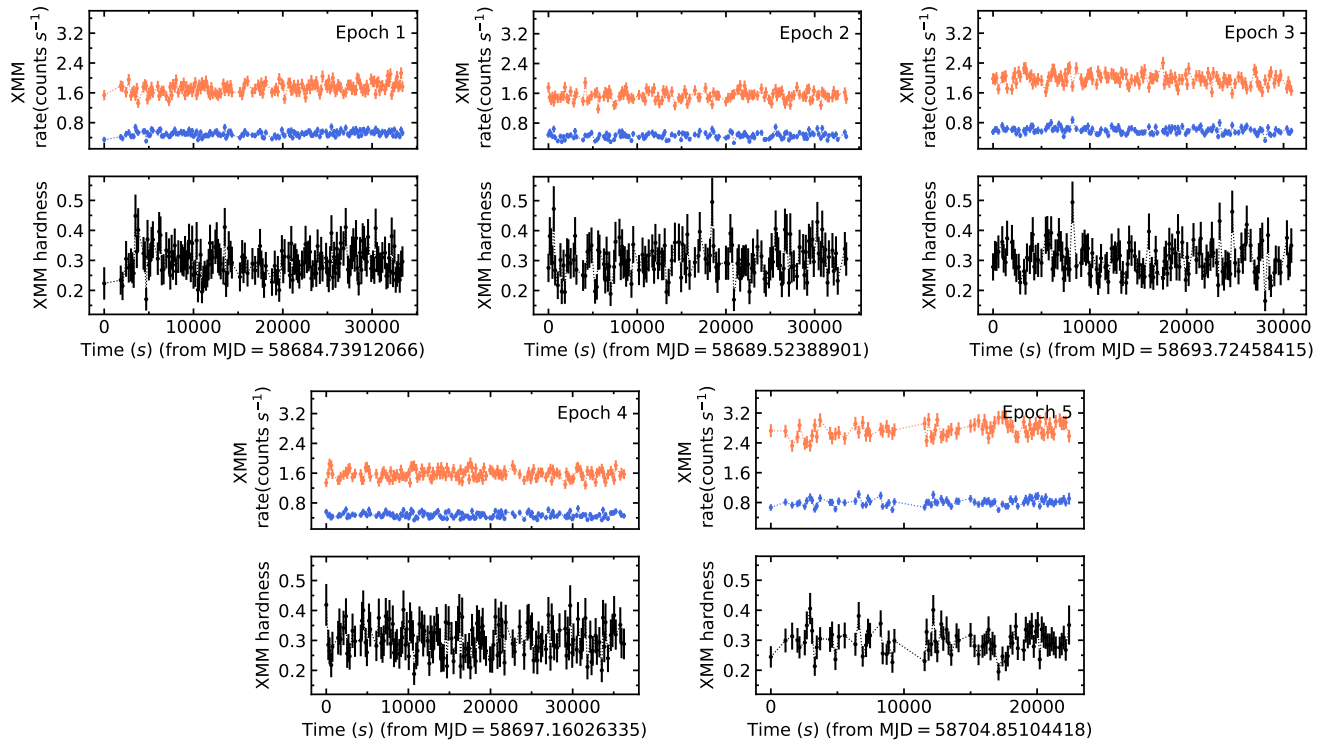


**Figure 3.** The light curves and corresponding hardness ratios extracted from the *XMM-Newton* observations in Epoch 1-5. The upper panels show the EPIC-pn light curves in the 0.3–2.0 keV (red) and 2–10 keV (blue) bands. The lower panels show the corresponding hardness ratios (2.0–10.0/0.3–2.0 keV). The bin time for the light curve is set to 150 s. The hardness ratio remains consistent between 0.2 and 0.4 in all epochs.

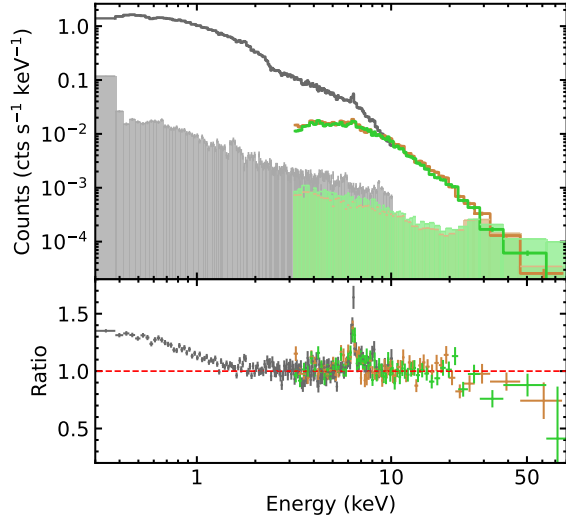


**Figure 4.** Top: *NuSTAR* (orange: FPMA; green: FPMB) and *XMM-Newton* (gray: EPIC-pn) source (crosses) and background spectra (shaded regions) of ESO 511–G030. Bottom: data-to-model ratio using an absorbed power-law model: grey for *XMM-Newton* data, orange and green for *NuSTAR* FPMA and FPMB data, respectively. The spectrum is fitted ignoring the data below 3 keV, above 15 keV and the 5–7 keV band (i.e., ignoring the soft excess region, the iron emission band, and Compton hump). The spectrum of ESO 511–G030 shows evidence of strong soft excess emission below 2 keV, iron K emission line at  $\sim 6.4$  keV, and a cutoff at high energies. The data have been rebinned for visual clarity.

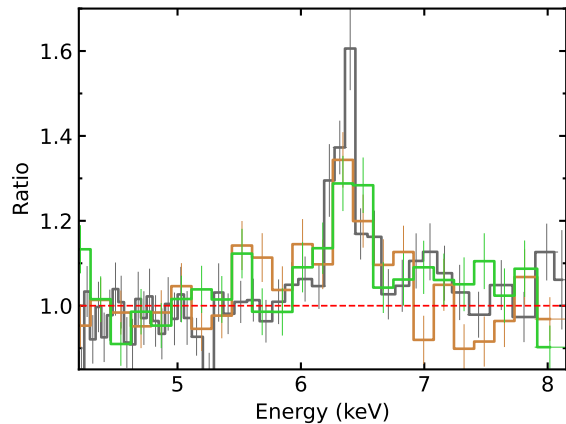


**Figure 5.** A detailed view of the region near the iron K emission line at 6.4 keV in Fig. 4. As in Fig. 4, the *XMM-Newton* data are shown in grey, *NuSTAR* FPMA data in orange and *NuSTAR* FPMB data in green. The *XMM-Newton* and *NuSTAR* spectra show a consistent shape for the narrow iron K-shell emission line. The data have been rebinned for visual clarity.

$\text{zms} \times (\text{bbody} + \text{nthcomp} + \text{xillverCp})$ . In our spectral analysis, the fit is insensitive to the inclination angle, so we fix it to a best-fit value  $i = 73^\circ$ . We also fix inclination angle at some other lower values and we get consistent results on the flux of *xillverCp*. In *nthcomp* model, we fix  $kT_{\text{bb}} = 10$  eV, which is the typical temperature for the accretion discs of AGNs and insensitive to the X-ray fitting processes (Done et al. 2012). The electron temperature  $kT_e$  and spectral slope  $\Gamma$  are linked to that in *xillverCp*. The best-fit results are shown in the third column of Tab. 3 and the uppermost panel of Fig. 6 shows the corresponding data-to-model ratio and the zoomed-in version of the residuals in the 6 keV region.

Model 1 shows that the phenomenological blackbody model can fit the spectra well from a statistical point of view, with a good fit statistic  $\chi^2_{\text{red}} \sim 1.106$ . The fitting requires a Galactic column density value of  $N_{\text{H}} = 0.041 \times 10^{22} \text{ cm}^{-2}$ , which is consistent with the results in Dickey & Lockman (1990) and Willingale et al. (2013). We set the ionization parameter as free and we get a value  $\log \xi < 0.5$ , hitting the lower limit  $\log \xi = 0.0$ . From the upper right panel of Fig. 6, we can conclude that model 1 describes the iron emission region well with a neutral distant reflection model, although we can still see some systematic residuals around the Fe K energies, i.e. around 8 keV, which is the blue wing of a potential broad iron line (can be confirmed with model 3). The best-fit model gives a blackbody temperature  $kT_{\text{bb}} = 0.143$  keV, which is in the range of characteristic temperature over a wide range of AGN luminosities and black hole masses (e.g., Walter & Fink 1993; Gierliński & Done 2004a; Bianchi et al. 2009; Crummy et al. 2006). The observed range in its temperature is very small, despite large changes in black hole mass, luminosity and spectral index across the AGN sample. Besides, this temperature ( $\sim 0.143$  keV) is too hot for the disc at a sub-Eddington rate ( $\lambda_{\text{Edd}} = 0.2\%$ , see Sec. 4 for detail) (Gierliński & Done 2004b). Then, it favors an origin through atomic processes instead of purely continuum emission (e.g., Gierliński & Done 2004a; Crummy et al. 2006).

The most peculiar aspect of this model is the relatively low temperature of the hot corona ( $kT_e = 13.2^{+2.5}_{-1.7}$  keV), which is uncommon for AGNs (e.g., Nandra & Pounds 1994; Ricci et al. 2017; Baloković et al. 2020; Kang & Wang 2022; Kamraj et al. 2022). To check the potential degeneracy between the coronal temperature and the strength of reflection, we test the constraints on corona temperature ( $kT_e$ ) and reflection fraction, presented in the upper panel of Fig. 7. Note that reflection fraction represents the so-called observer’s re-

flection fraction (Ingram et al. 2019) in our analysis, and is defined as the observed reflected flux divided by the observed hot coronal flux in the 0.3–80 keV band. From the contour plot, we find both parameters are tightly constrained, and there is not any degeneracy between two parameters. We now implement some more physically motivated model to study the soft excess and the excess around 6-7 keV.

### 3.2. Model 2: warm corona model

A warm ( $T_e \sim 10^{5-6}$  K) and optically thick ( $\tau \sim 10-40$ ) corona model has been proposed to explain the observed soft excess in AGNs (e.g., Magdziarz et al. 1998; Petrucci et al. 2018; Porquet et al. 2018; Middei et al. 2020). In this scenario, the soft excess is the high-energy tail of the resulting spectrum of a warm corona. This corona may be an extended, slab-like plasma at the upper layer of the disc, which is cooler than the hot ( $T_e \sim 10^{8-9}$  K), centrally located, and more compact corona responsible for the non-thermal power-law continuum.

Based on model 1, in model 2 we replace `tbody` with the physically motivated model `nthcomp` to represent the warm corona. In this case, the model reads as `tbnew × zmsift × (nthcomp1+nthcomp2+xillverCp)` in XSPEC language. `nthcomp1` is to model the soft excess and `nthcomp2` is to model the hot corona. To model the reflection spectrum, we still use `xillverCp` with  $F_{\text{ref}}$  fixed to  $-1$ . `nthcomp` is characterized by the continuum slope,  $\Gamma$ , the temperature of the covering electron gas,  $kT_e$ , and the seed photon temperature,  $kT_{\text{bb}}$ . We fix  $kT_{\text{bb}} = 10$  eV for `nthcomp1` and `nthcomp2`. The electron temperature  $kT_e$  and spectral slope  $\Gamma$  are set to be variable in `nthcomp1`. And the electron temperature  $kT_e$  and spectral slope  $\Gamma$  of `nthcomp2` are linked to that in `xillverCp`.

The warm corona model results in a fit statistic  $\chi_{\text{red}}^2 \sim 1.113$  (see the fourth column of Tab. 3) and models the residuals in Fig. 4 well (the middle panel of Fig. 6). The spectral slope found for the warm corona is  $\Gamma = 2.6_{-0.4}^{+0.4}$  and the estimate of the temperature is  $0.1908_{-0.04}^{+0.0009}$ , which is consistent with the range (0.1  $\sim$  1 keV) reported in Petrucci et al. (2018). By comparison, the hot corona is characterized by a more gentle spectral slope ( $\Gamma = 1.716_{-0.009}^{+0.009}$ ) and a higher temperature ( $kT_e = 13.23_{-0.9}^{+0.21}$  keV), which are almost identical to model 1. The middle panel of Fig. 7 shows the constraints on the temperature of the hot corona ( $kT_e$ ) and the reflection fraction for model 2.

### 3.3. Model 3: relativistic reflection model

The other popular explanation of the soft excess is the relativistic disc reflection model (e.g., Crummy et al.

2006; Fabian et al. 2009; Walton et al. 2013; Jiang et al. 2018). In the strong gravitational field of supermassive black holes, the fluorescent features radiated on the inner region of the accretion disc are blurred (Fabian et al. 2005). Moreover, it has recently been shown that the existence of the enhanced inner-disc density, above the commonly assumed value of  $n_e = 10^{15} \text{ cm}^{-3}$  (e.g., Ross & Fabian 1993, Ross & Fabian 2005; García et al. 2011), results in an increased emission at soft energies ( $< 2$  keV). This occurs because at high densities free-free heating (bremsstrahlung) in the disc atmosphere becomes dominant and results in an increased gas temperature (García et al. 2016; Jiang et al. 2019c). As a consequence, relativistic reflection from a highly dense disc can lead to increased low-energy emission, which may account for the soft excess.

To test this explanation, We implement the reflection model `xillverDCp`<sup>1</sup>, a version of `xillver` that allows for variable disc density, convolved by `relconv` (Dauser et al. 2013) to model the relativistic reflection component. And the bare `xillverCp`, in which electron density is fixed at  $n_e = 10^{15} \text{ cm}^{-3}$ , is reserved for the distant non-relativistic reflection component. From the view of self-consistent model, the parameters  $F_{\text{ref}}$  of the two reflection models are fixed as  $-1$  to return only the reflection component, and a non-thermal power-law continuum model `nthcomp` is included to account for the power-law component from the hot corona. In XSPEC language, the model combination is `tbnew × zmsift × (relconv × xillverDCp + nthcomp + xillverCp)`. Same as model 2, we fix  $kT_{\text{bb}} = 10$  eV for `nthcomp`. For the spectral slope  $\Gamma$  and electron temperature  $kT_e$ , the hot corona, relativistic disc reflection, and distant reflection components are tied together. And for `xillverCp` and `xillverDCp`, the inclination angles are linked to the same parameter in `relconv`. The ionization parameter is set to its minimum ( $\xi = 0 \text{ erg cm s}^{-1}$ ) in `xillverCp` and free in `xillverDCp`. Similarly, the electron density is set to its minimum ( $n_e = 10^{15} \text{ cm}^{-3}$ ) in `xillverCp` and free in `xillverDCp`. The inner radius  $R_{\text{in}}$  and the outer disc radius  $R_{\text{out}}$  of the accretion disc are fixed at their default value, i.e.,  $R_{\text{in}} = R_{\text{ISCO}}$  and  $R_{\text{out}} = 400R_g$  ( $R_g = GM/c^2$ , gravitational radii). We assume that the emissivity profile follows a  $q = 3$  power law and the spin parameter is fixed at the maximum value  $a_* = 0.998$  in `relconv` because of its insensitivity to the fit, and the disc inclination angle varies freely. The iron abundance of `xillverCp` is linked to that in `xillverDCp`.

<sup>1</sup> <https://sites.srl.caltech.edu/javier/xillver/index.html>

**Table 3.** Best-fit values for model 1, model 2 and model 3.

		Model 1	Model 2	Model 3
Model	Parameter			
<b>tbnew</b>	$N_{\text{H}}$ ( $10^{22}$ cm $^{-2}$ )	$0.041^{+0.009}_{-0.007}$	$0.061^{+0.003}_{-0.013}$	$0.034^{+0.005}_{-0.004}$
<b>bbody</b>	$kT$ (keV)	$0.143^{+0.017}_{-0.011}$	-	-
<b>nthcomp</b>	$\Gamma$	-	$2.6^{+0.4}_{-0.4}$	-
	$kT_e$ (keV)	-	$0.1908^{+0.0009}_{-0.04}$	-
<b>relconv</b>	$a^*$	-	-	$0.998^*$
<b>xillverDCp</b>	$\log n_e$	-	-	$18.1^{+0.4}_{-1.0}$
	$\log \xi$	-	-	$1.0^{+0.6}_{-0.7}$
<b>nthcomp</b>	$\Gamma$	$1.716^{+0.01}_{-0.009}$	$1.716^{+0.009}_{-0.009}$	$1.753^{+0.014}_{-0.02}$
	$kT_e$ (keV)	$13.2^{+2.5}_{-1.7}$	$13.23^{+0.21}_{-0.9}$	$13.8^{+2.5}_{-1.9}$
<b>xillverCp</b>	$A_{\text{Fe}}$	$10.0^{+P}_{-1.5}$	$10.0^{+P}_{-0.9}$	$8.1^{+P}_{-3}$
	$i$ (deg)	$73^*$	$73^{+7}_{-15}$	$72.6^{+4}_{-5}$
	$\log \xi$	$0.0^{+0.5}_{-P}$	$0.0^{+0.4}_{-P}$	$0^*$
	$C_{\text{FPMA}}$	$1.247^{+0.023}_{-0.022}$	$1.247^{+0.016}_{-0.016}$	$1.248^{+0.022}_{-0.022}$
	$C_{\text{FPMB}}$	$1.226^{+0.023}_{-0.022}$	$1.226^{+0.016}_{-0.016}$	$1.228^{+0.022}_{-0.022}$
	$F_{\text{bbbody}} (\times 10^{-13})$	$2.6^{+1.0}_{-0.9}$	-	-
	$F_{\text{WC}} (\times 10^{-13})$	-	$4.7^{+1.3}_{-1.8}$	-
	$F_{\text{xillverCp}} (\times 10^{-13})$	$5.9^{+1.7}_{-0.8}$	$5.9^{+0.6}_{-0.6}$	$6.2^{+2.5}_{-1.5}$
	$F_{\text{HC}} (\times 10^{-11})$	$1.55^{+0.06}_{-0.03}$	$1.51^{+0.05}_{-0.04}$	$1.41^{+0.06}_{-0.06}$
	$F_{\text{RR}} (\times 10^{-12})$	-	-	$1.2^{+0.3}_{-0.3}$
	$\chi^2/\text{d.o.f}$	646.39/585	649.51/584	648.11/584

*Note.* The flux (0.3–80 keV) of the each component are presented in units of erg s $^{-1}$  cm $^{-2}$ .  $F_{\text{WC}}$ ,  $F_{\text{HC}}$  and  $F_{\text{RR}}$  represent the flux of the warm corona component, the hot corona component and the relativistic reflection component, respectively.  $\xi$  in units of erg cm s $^{-1}$ .  $n_e$  in units of cm $^{-3}$ .

The best-fit values are listed in the fifth column of Tab. 3 and the residuals are shown in the lower panel of Fig. 6. The relativistic reflection picture provides a better fit than the warm corona model, with  $\chi^2_{\text{red}} \sim 1.110$ . Compared with the warm corona model, the relativistic reflection model slightly improves the fit with  $\Delta\chi^2 = 1.95$ . As shown in the fifth column of Tab. 3, this model gives essentially similar results to those reported in model 1 and model 2. With such a relativistic reflection model, the iron complex region is modeled better as shown in the lower right panel of Fig. 6. Same as the previous 2 models, this model provides a low temperature

for the hot corona as well. The constraints on the temperature of the hot corona ( $kT_e$ ) and reflection fraction are presented in the lower panel of Fig. 7. Here, the reflection fraction is flux ratio between the relativistic reflection component (dominates in 0.3–80 keV band) and the hot corona component. We test the constraints on corona temperature ( $kT_e$ ) and photo index ( $\Gamma$ ) to check the potential degeneracy in this parameter plane. The results are presented in Fig. 8. It shows that there is not significant degeneracy between  $kT_e$  and  $\Gamma$  in all models. We also find that a high inclination is preferred



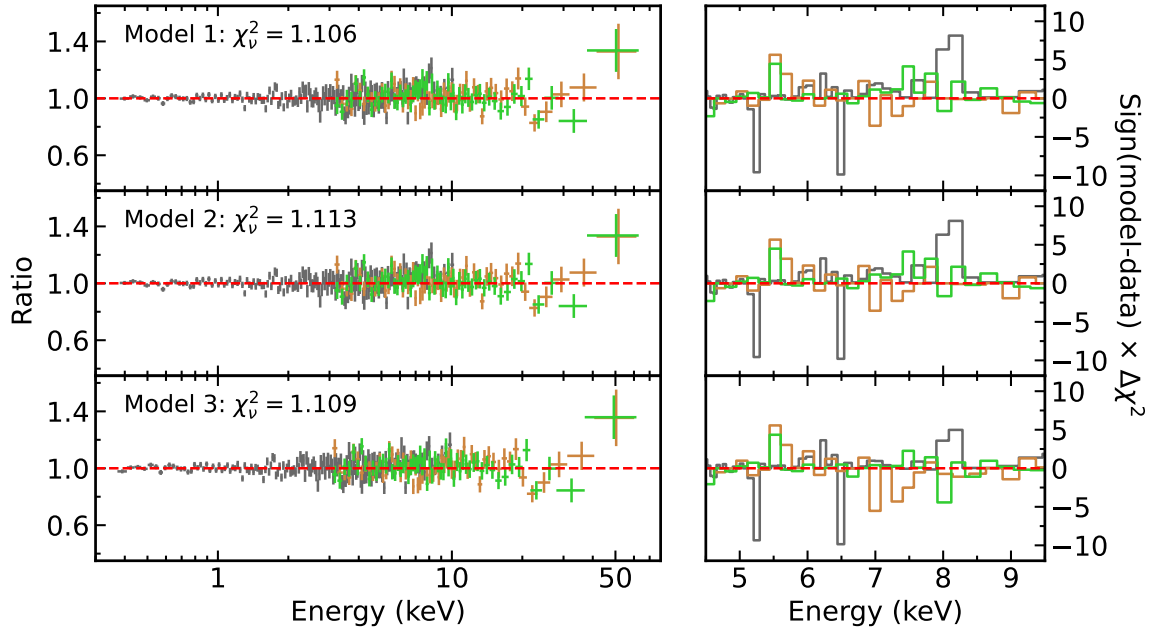


**Figure 6.** Left: Data-to-model ratios for the blackbody model (model 1, top), the warm corona model (model 2, middle), and the relativistic reflection model (model 3, bottom). The *XMM-Newton* *NuSTAR*/FPMA data and *NuSTAR*/FPMB are marked with gray, orange and green crosses respectively. Right: The zoom-in residuals between 4.5–9.5 keV. The best-fit models are shown in Fig. 10.

by 3 models, though it can not be constrained well in model 1 (Fig. 9).

In the fit of model 3, we model the emissivity profile of the disc with a power-law mode with  $q_{\text{in}} = q_{\text{out}} = 3$ . If we free  $q_{\text{in}}$  and  $q_{\text{out}}$  in the fit, we find that these two parameters are insensitive to the fit. So we do not explore further such a possibility.

#### 4. DISCUSSION

In the previous sections, we presented the spectral properties of the AGN ESO 511–G030, and found that the variability mainly happens over the entire broadband spectrum, and the hardness ratio curve remains constant. With a simple absorbed power-law model, the typical AGN spectral features—a soft excess below  $\sim 2$  keV, Fe  $K\alpha$  emission at  $\sim 6.4$  keV, and a cutoff at high energy, are revealed. The soft excess can be modeled by a single temperature blackbody model `tbody` with a typical temperature  $kT_{\text{bb}} = 0.143$  keV, and iron emission can be modeled by a simple gaussian model with centroid energy  $E = 6.39$  keV in the rest frame of the object and line width  $\sigma = 0.04^{+0.05}_{-0.03}$  keV, based on which we identify this line as Fe  $K\alpha$  emission line and an origin of a distant reflector.

We carry out spectral analyses based on two different hypotheses to explain the soft excess: the warm corona and the relativistic reflection scenario. In the process of fitting with the warm corona model, the introduction of a soft ( $\Gamma = 2.6$ ), cool temperature ( $kT_e = 0.1908$  keV)

model `nthcomp` yields good results. In the process of fitting with the relativistic reflection model, we utilize the `xillver`-based model and this model provides somewhat satisfactory fits to the spectra. In this section, we discuss the physical aspects of previous fits and the exploration of further study.

##### 4.1. Eddington ratio estimation

We calculate the Eddington ratio  $\lambda_{\text{Edd}}$  of ESO 511–G030 by applying an average bolometric luminosity correction factor  $\kappa = 20$  (Vasudevan & Fabian 2007) to the 2–10 keV band unabsorbed luminosity  $5.56 \times 10^{42}$  erg  $\text{s}^{-1}$ . A black hole mass of  $\sim 4.57 \times 10^8 M_{\odot}$  (Ponti et al. 2012) is considered. We obtain  $\lambda_{\text{Edd}} = \kappa L_X / L_{\text{Edd}} = 0.002$ , which is consistent with the results reported in Ghosh & Laha (2021). Ghosh & Laha (2021) analyzed the broadband spectra observed by *XMM-Newton* and *Suzaku*, and reported that the source was accreting at a sub-Eddington rate ( $\lambda_{\text{Edd}}$  varies within 0.002 - 0.008) between 2007 and 2012. They also reported a power-law continuum with a photon index varying between  $\Gamma = 1.7 - 2.0$ , and the presence of a broad Fe emission line at  $\sim 6.4$  keV in the source spectra with  $\sigma = 0.08 - 0.14$  keV. It seems that the profile of Fe emission line is related to the flux state of the source. We will conduct a detailed investigation of the variability and spectral properties of different flux states in a forthcoming paper.

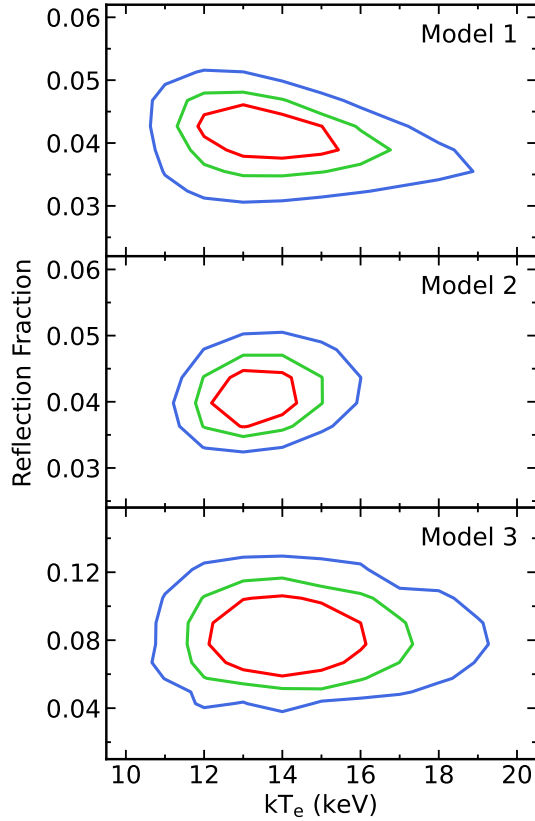


**Figure 7.** Constraints on temperature of hot corona ( $kT_e$ ) and . For model 3, the reflection fraction is defined with the method in text. The constraints on  $kT_e$  are consistent from the various model. The red, green, and blue curves represent, respectively, the 68%, 90%, and 99% confidence level limits for two relevant parameters ( $\Delta\chi^2 = 2.30, 4.61,$  and  $9.21,$  respectively).

#### 4.2. Model the background spectra

As shown in Fig. 4, the hard X-ray spectral shape of ESO 511–G030 depends on the accuracy of the background modelling on *NuSTAR*. To avoid the influence of uncertainty from the background, we carefully choose the background region and use the most strict filtering criteria to filter the data. Moreover, we conduct a detailed analysis of background spectra and the uncertainty from the background spectrum. To do so, we use the toolkit named “nuskybgd” (Wik et al. 2014). Thanks to nuskybgd, we can construct the background spectra for any region in which we are interested.

As is typical, the background has both intrinsic and extrinsic components. The nuskybgd model consists of four components, which combine to fully describe the background:

$$B_d(E, x, y) = A_d(E, x, y) + f_d(E, x, y) + S_d(E) + I_d(E)$$

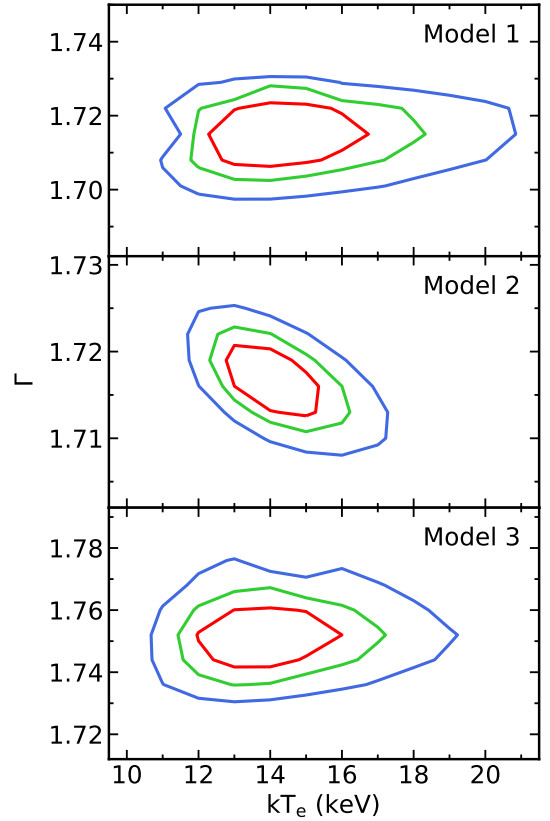


**Figure 8.** Constraints on temperature of hot corona ( $kT_e$ ) and photo index ( $\Gamma$ ). The red, green, and blue curves represent, respectively, the 68%, 90%, and 99% confidence level limits for two relevant parameters ( $\Delta\chi^2 = 2.30, 4.61,$  and  $9.21,$  respectively).

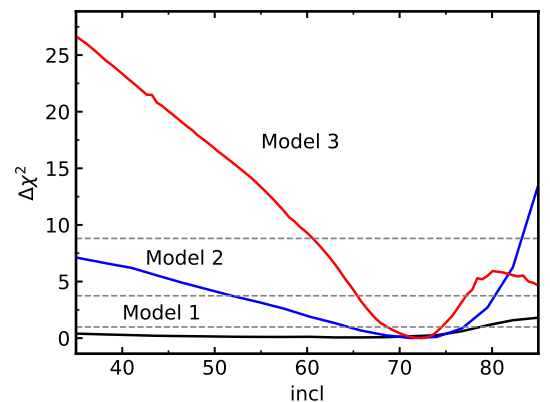


**Figure 9.** The  $\Delta\chi^2$  contours for the inclination parameters for all 3 models. The gray horizontal lines represent the  $1\sigma,$   $2\sigma$  and  $3\sigma$  confidence levels from the bottom up for a single parameter of interest.

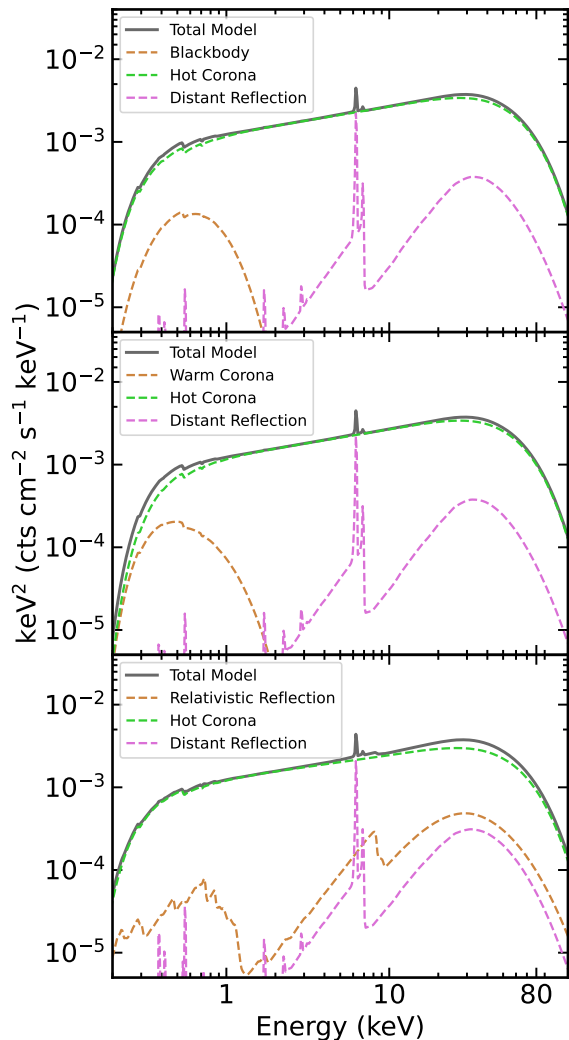


**Figure 10.** Model components of the best-fit model in the blackbody model (model 1, top), the warm corona model (model 2, middle), and the relativistic reflection model (model 3, bottom).

$A_d(E, x, y)$  describes the stray-light cosmic X-ray background (CXB) through the aperture, marked by "aCXB";  $f_d(E, x, y)$  describes the focused CXB, marked by "fCXB";  $S_d(E)$  describes instrument line emissions and reflected solar X-rays, marked by "Inst";  $I_d(E)$  describes the instrument Compton scattered continuum emissions, marked by "Intn". Using the ftool included in `nuskybgd`, we can fit the background spectrum by the model above. Based on the best-fit parameters, the background image and the background spectrum for an arbitrary region in the FOV can be produced.

Our background estimation of ESO 511–G030 with *NuSTAR* is as follows. We extract the FPMA and FPMB background spectra for Epoch 1-5 separately, according to the strategy in Sec. 2. And then fit the back-

ground spectra with the standard `nuskybgd` model. The spectra of Epoch 1 are shown with all the components of the background model in Fig. 11. The background spectra are well-fitted by our background model. To construct the background spectrum for the region of interest, we use the ftool `nuskybgd-spec` in `nuskybgd` for aCXB, fCXB, Inst, and Intn components. The background is estimated based on the best-fit parameters of the background spectrum for the region of interest. Thus, we simulate FPMA and FPMB background spectra for every epoch, which is 10 times the exposure time of the original observation. Because the model for background spectra is complex, the error would be very large if the exposure is too short. Simulated background spectra are merged to an averaged spectra for FPMA and FPMB separately. We replace the background spectra with the simulated one in model 1 to estimate the uncertainty from the background. Fig. 12 compares the measurements using two methods. An almost identical constraint is given with the simulated background.

As shown in Fig. 11, at higher ( $E > 30$  keV) energies, internal  $I_d(E)$  term strongly dominates the background spectra. The remainder of the internal background consists of various activation and fluorescence lines, which are mostly resolved and only dominate the background between 22–32 keV. Above these energies, weaker lines are still present, but the continuum dominates. There is no dependence on pixel location  $x, y$ , only on energy  $E$ , so the spatial distribution across a given detector is uniform. and for internal background, the systematic uncertainty could in theory be arbitrarily close to 0% (Wik et al. 2014; Tsuji et al. 2019), or at least has the least uncertainty compared to other components. In summary, *NuSTAR* observation supply the relatively reliable broadband spectra from 3.0–78.0 keV, although the background plays an important role in the high energy band.

#### 4.3. Physical properties of the warm corona model

In the fit of model 2, the warm corona model with a hot corona and a neutral distant reflection component describes the observational data well. The corresponding optical depth of the warm corona ( $\tau \sim 18 - 25$ ), calculated with Eq. (13) in Beloborodov (1999a), i.e.,  $\Gamma \simeq \frac{4}{9}y^{-\frac{2}{3}}$  with  $y = 4[kT_e/m_e c^2 + (kT_e/m_e c^2)^2]\tau(\tau + 1)$  the so-called Compton parameter. Petrucci et al. (2018) test the warm corona model on a statistically significant sample of unabsorbed, radio-quiet AGNs with *XMM-Newton* archival data and find the temperature of the warm corona to be uniformly distributed in the 0.1–1 keV range, while the optical depth is in the range  $\sim 10$ –40. The observational characteristics of the warm

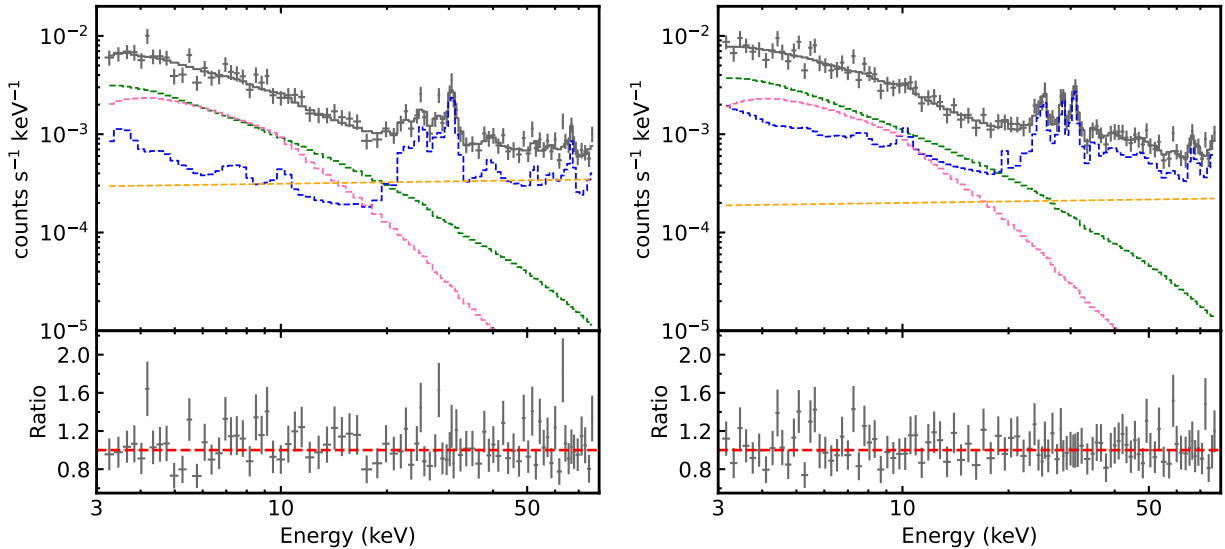


**Figure 11.** Left: the background spectrum of *NuSTAR* FPMA ( Obs ID: 60502035002) with `nuskybgd` model. The black, green, pink, blue, and orange lines, respectively, indicate the total background, aCXB, fCXB, Inst, and Intn, included in `nuskybgd`. Right: the background spectrum of *NuSTAR* FPMB of the same observation. Each component is shown with same color as left.

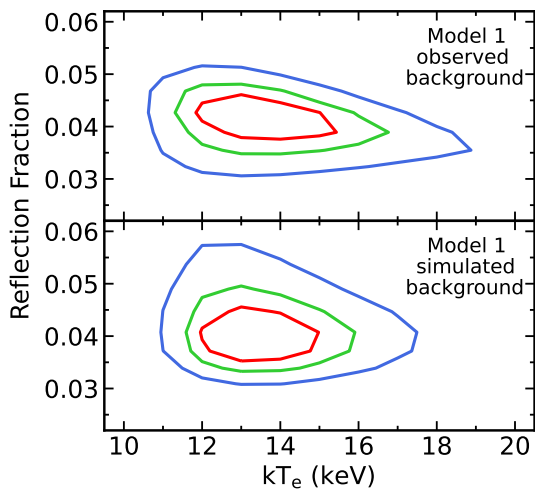


**Figure 12.** Constraints on temperature of hot corona and reflection fraction with model 1. Upper panel show the results using observed background. Lower panel show the results using simulated background. The red, green, and blue curves represent, respectively, the 68%, 90%, and 99% confidence level limits for two relevant parameters ( $\Delta\chi^2 = 2.30, 4.61, \text{ and } 9.21$ , respectively).

corona (i.e., a photon index of 2.5 and a temperature of 0.1–2 keV) is within the prediction of [Petrucci et al. \(2018\)](#) ( $\tau \sim 10\text{--}40$ ), and agree with an extended warm corona covering the disc which is mainly nondissipative ([Petrucci et al. 2018](#), later corrected in [Petrucci et al. 2020](#)).

With the warm corona scenario, we get a slightly harder slope of the continuum  $\Gamma = 1.716$ , compared with model 3. Similar results were also be found in [García](#)

[et al. \(2018\)](#), and [Xu et al. \(2021\)](#). It means that the warm corona scenario requires a harder continuum in the absence of the compensation of the high energy photons from the inner disc reflection. In our fits, the difference in the photon index between the warm corona and relativistic reflection is  $\Delta\Gamma \sim 0.04$ . For the given X-ray AGN spectrum data with the soft excess, the lack of any disc reflection component in the pure warm corona model is likely to provide a harder continuum than the relativistic reflection explanation.

However, [Gronkiewicz & Różańska \(2020\)](#) computed the transition from the disc to corona, using the vertical model of the disc supported and heated by the magnetic field together with radiative transfer in hydrostatic and radiative equilibrium. They concluded that the radial extent of the warm corona is limited by local thermal instability and a warm corona like this is stronger in the case of a higher accretion rate and a greater magnetic field strength. So thermal instability should prevent the warm corona from forming for lower accretion rate system. The low accretion rate system is unable to provide enough energy to sustain a warm corona ([Ballantyne & Xiang 2020](#)). It is therefore unclear whether a strong warm corona can be sustained at the low accretion rates relevant here ( $\dot{m} \sim 0.002$ ). This may imply that even if a warm corona is present, a contribution from the disc reflection would be necessary to produce the observed strong soft excess.

#### 4.4. Physical properties of the relativistic disc reflection

The high-density disc reflection model proposed in [García et al. \(2016\)](#) is based on an extended model of the standard accretion disc. [García et al. \(2016\)](#) demonstrated that if the disc density is higher than the typically fixed value  $n_e = 10^{15} \text{ cm}^{-3}$ , the main effect is the enhancement of the reflected continuum at low energies, further enhancing the soft excess. We note that the relativistic reflection model produces a similar statistical result to the warm corona model for ESO 511–G030, with consistent key parameters.

The relativistic reflection explanation requires a dense accretion disc with density  $\log[n_e/\text{cm}^{-3}] = 18.1^{+0.4}_{-1.0}$ . This result is consistent with previous findings that a larger gas density than the previously adopted value of  $\log[n_e/\text{cm}^{-3}] = 15$  is usually required for SMBHs with  $\log[m_{\text{BH}}/M_\odot] \leq 8$ , like Ark 564 ([Jiang et al. 2019c](#)) and ESO 362–G18 ([Xu et al. 2021](#)). Another factor that affects the expected disc density is the accretion rate. According to the standard thin disc model ([Shakura 1973](#)), [Svensson & Zdziarski \(1994\)](#) derived a relationship between the density  $n_e$  of a radiation-pressure-dominated disc and the accretion rate  $\dot{m}$ ,

$$n_e = \frac{1}{\sigma_T R_S} \frac{256\sqrt{2}}{27} \alpha^{-1} R^{3/2} \dot{m}^{-2} \left[1 - \left(\frac{R_{\text{in}}}{R}\right)^{1/2}\right]^{-2} [\xi(1-f)]^{-3},$$

where  $\sigma_T = 6.64 \times 10^{25} \text{ cm}^2$  is the Thomson cross-section;  $R$  is in the units of  $R_S$  (Schwarzschild radius);  $\xi$  is the conversion factor in the radiative diffusion equation and chosen to be 1, 2, or 2/3 by different authors;  $f$  is the fraction of the total transported accretion power released from disc to the hot corona. With the correlation formula  $\log[n_e] \propto -2 \log[\dot{m}]$ , they concluded that a lower accretion rate leads to a higher gas density. Similar conclusions were found in disc reflection modelling of black hole (BH) X-ray binaries ([Jiang et al. 2019a](#)) and other AGNs with a high BH mass (e.g. Mrk 509, [García et al. 2018](#)).

Another characteristic is the low ionization parameter of the relativistic reflection component, which indicates that the degree of ionization on the accretion disc is relatively low. [Ballantyne et al. \(2011\)](#) reported a positive statistical correlation between  $\xi$  and the AGN Eddington ratio  $\dot{m}$  based on the simple  $\alpha$ -disc theory. We plug the Eddington ratio  $\dot{m} = 0.002$  into Formula (1) of [Ballantyne et al. \(2011\)](#), and get the estimation of the ionization parameter through,  $\log \xi \sim 0.5$ . This value is smaller than our fitting results, but consistent within error. The physical interpretation is that the accretion rate affects the fraction of the accretion energy dissipated in the corona (e.g., [Svensson & Zdziarski 1994](#); [Merloni & Fabian 2002](#); [Blackman & Pessah 2009](#)), which emits X-ray photons to photoionize the inner disc

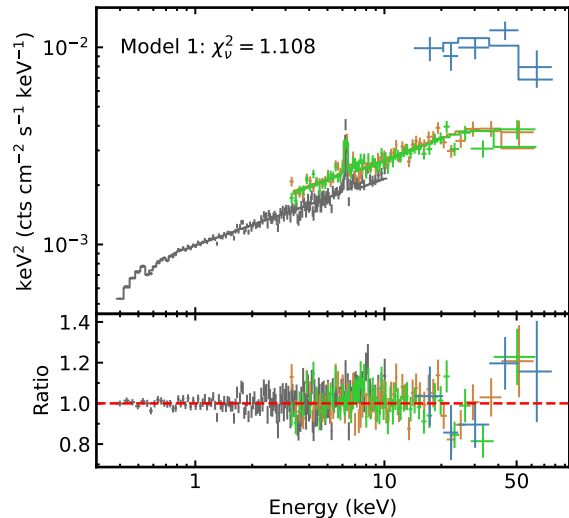


**Figure 13.** The spectrum and the corresponding residuals with model 1, considering *Swift*/BAT spectrum (blue). The *XMM-Newton NuSTAR*/FPMA data and *NuSTAR*/FPMB are marked with gray, orange and green crosses respectively.

surface. All models show a low reflection fraction, which recall the case of an outflowing corona ([Beloborodov 1999b](#); [Malzac et al. 2001](#)). This can be confirmed by future missions.

We explore the possibility of measuring the spin with this model. The result is that the spin parameter cannot be constrained in `relconv`. With one more free parameter, we slightly improve the fit with  $\Delta\chi^2 = 0.95$  and only have a lower limit ( $a_* > -0.58$ ).

#### 4.5. Low-temperature corona in sub-Eddington accretors

The most striking discovery is the relatively low temperature of the hot corona, which is confirmed by all broadband models, as shown in Fig. 7. To seek any possible variability of the temperature of coronae in a long timescale, we fit the *Swift* 70-month BAT spectrum ([Baumgartner et al. 2013](#)) together with the *XMM-Newton* and *NuSTAR* spectrum. The ratio plot is shown in Fig. 13, fitted with model 1. The *Swift* BAT spectrum shows a consistent shape with the *NuSTAR* FPM spectra above 30 keV, and we get an almost identical fitting results. The cross-calibration constant for BAT is 3.64.

[Fabian et al. \(2015\)](#) compiled a sample of all the high energy cut-offs observed with *NuSTAR* and populated these sources on the compactness-temperature ( $l$ - $\Theta$ ) plane, where  $\Theta = kT_e/m_e c^2$  is the coronal electron temperature normalized by the electron rest energy and  $l = (L/R)(\sigma_T/m_e c^3)$  is the dimensionless compactness parameter ([Guilbert et al. 1983](#)). [Fabian et al. \(2015\)](#)



defined  $L$  as the luminosity of the power-law component from 0.1–200 keV and  $R$  as the radius of the corona (assumed spherical).

The allowed parameter space in the  $\ell$ - $\Theta$  plane is limited by theoretical constraints, like the pair balance line that is estimated by Svensson (1984). With more power is fed into the corona, electron temperature  $\Theta = kT_e/m_e c^2$  rises, and Compton scattering of the soft photons produces a power-law radiation spectrum extending to a Wien tail at energies around  $2\Theta$ . When the tail extends above  $\sim 2m_e c^2$ , photon–photon collisions happen and create electron–positron pairs. Thus any additional energy input will lead to an increased number of pairs, but does not increase the source temperature. Fabian et al. (2015) analyzed all sources observed up to that point by *NuSTAR* and found nearly all sources lay just below the pair-production limit for thermal Comptonization, suggesting that these coronae are pair-dominated plasmas.

To compare our results of ESO 511–G030 with the results of Fabian et al. (2015), we conduct the same analysis with the result of model 3. With model 3, we get an electron temperature of 13.8 keV ( $\Theta = 0.027$ ). Following Fabian et al. (2015), we measure the Comptonization component from 0.1–200 keV to be  $1.95 \times 10^{43}$  erg s $^{-1}$ . For simplicity, we assume a value of  $R = 10R_g$ , which is a conservative assumption given the measurements. This leads to a compactness of  $\ell = 4.4$ . ESO 511–G030 lies well below the thermal pair-production limit and above the  $e^- - p$  coupling line (Fig. 14), and thus, assuming a thermal Comptonization model, we find that the corona in this source is a pair-dominated plasma. However, Fabian et al. (2017) re-examined the case of hybrid coronae (Zdziarski et al. 1993), where the plasma contains both thermal and non-thermal particles, as might be expected for a highly magnetized corona powered by the dissipation of magnetic energy. Searching the position in Fig. 6 of Fabian et al. (2017), we find the corona of ESO 511–G030 is prone to a hybrid plasma with large fraction of electrons following a non-thermal distribution, as shown in Fig. 15. Further deep hard X-ray observations are required to distinguish these two scenarios.

Peculiarly, a low coronal temperature is seen in only a handful of AGN, such as 1H0419–577 ( $kT_e = 30^{+22}_{-7}$  keV; Jiang et al. 2019b), Ark 564 ( $kT_e = 15 \pm 2$  keV; Kara et al. 2017), GRS 1734–292 ( $kT_e = 11.9^{+1.2}_{-0.9}$  keV; Tortosa et al. 2017), IRAS 13197–1627 ( $kT_e < 42$  keV; Walton et al. 2018), 4C 50.55 ( $kT_e \approx 30$  keV; Tazaki et al. 2010), IRAS 04416+1215 ( $kT_e = 3 \sim 20$  keV; Tortosa et al. 2022), ESO 362–G18 ( $kT_e \approx 20$  keV; Xu et al. 2021) and 3C 273 ( $kT_e = 12 \pm 1$  keV;

Madsen et al. 2015b). Note that except the Seyfert 1 galaxy GRS 1734–292 ( $\lambda_{\text{Edd}} \sim 0.03$ ), the Seyfert 1.5 Galaxy ESO 362–G18 ( $\lambda_{\text{Edd}} \sim 0.02$ ) and the Seyfert 1.8 Galaxy IRAS 13197–1627 ( $\lambda_{\text{Edd}} \sim 0.05$ –0.1), all the other sources mentioned above are accreting at a significant fraction of Eddington. In this work, we find another source with a low-temperature corona in a significantly sub-Eddington regime. For high-Eddington accreting system, the sources would be cooled by relatively cooler seed photons, thus producing the lower temperature cut-off that is observed (e.g., Kara et al. 2017). Inversely, the accretion rate of ESO 511–G030 is only a few per cent of the Eddington limit, so the effectiveness of the cooling mechanism cannot be related to a particularly strong radiation field. However, the high value of the optical depth  $\tau$  could be, at least, partly responsible for effectiveness of the cooling mechanism in such sub-Eddington regime (Kamraj et al. 2022). Indeed, models predict an anticorrelation between coronal temperature and optical depth (e.g. Petrucci et al. 2001). But the reason for the unusually large value of the optical depth is unclear (Tortosa et al. 2017).

The differences between the possible physical scenarios for the soft excess and low coronal temperatures are significantly much more evident outside the energy coverage and energy resolution of current observatories. With the increasing amount of high-quality spectra from *NuSTAR*, it would be possible to start seriously pondering these questions. It would be conclusively distinguished with future missions such as *Athena* (Nandra et al. 2013), eXTP (Zhang et al. 2016), XRISM (Tashiro et al. 2018) and HEX-P (Madsen et al. 2018), which are crucial for providing reliable high-resolution X-ray observations. In addition, HEX-P provides a broadband (2–200 keV) response and a much higher sensitivity than any previous mission in the hard energy band. The nature of the corona is likely to be determined by the high-quality observations performed by HEX-P.

## 5. CONCLUSIONS

We investigated the variability and spectra properties from the joint *XMM-Newton* and *NuSTAR* observing campaign on the Seyfert 1 Galaxy ESO 511–G030. Lightcurve and spectral analysis on its *XMM-Newton* and *NuSTAR* simultaneous observations show that:

1. The source remained in a relatively constant flux state throughout the observation period.
2. The broadband (0.3–78 keV) spectrum shows the presence of a power-law continuum with a soft excess below 2 keV, a relatively narrow iron K $\alpha$  emis-

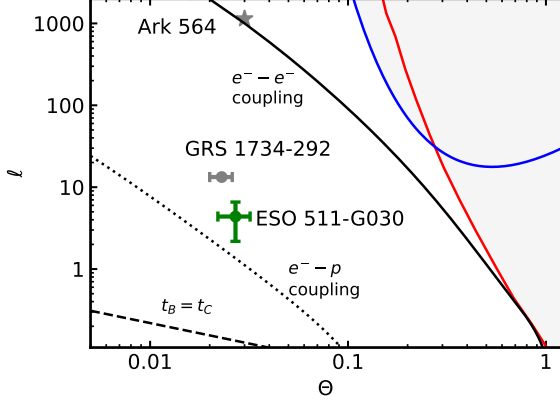


**Figure 14.** Theoretical compactness–temperature diagram. The green cross indicates the position of ESO 511–G030. The lines are summary of theoretical understanding of the  $\ell$ – $\Theta$  plane as described in Fabian et al. (2015); included are the boundaries for electron–electron coupling, electron–proton coupling, the dominance of Compton cooling and pair lines for different assumptions. The positions of GRS 1734–292 and Ark 564 are also indicated in the figure. Located on the similar position, ESO 511–G030 and GRS 1734–292 would have similar properties.

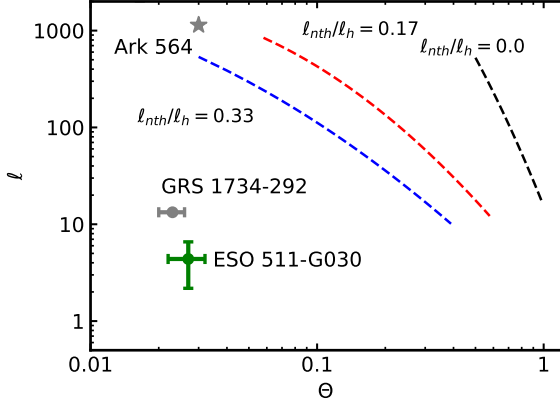


**Figure 15.** Theoretical compactness–temperature diagram. The green cross indicates the position of ESO 511–G030. The dashed lines are theoretical predictions of a hybrid plasma with  $\ell_h/\ell_s = 1$ , where  $\ell_h$  is the total heating parameter and  $\ell_s$  is the compactness of the soft photons. The blue, red and black lines represent solutions with a non-thermal fraction ( $\ell_{nth}/\ell_h$ ) of 0.33, 0.17 and 0.0 respectively (see Fabian et al. (2017)).

sion ( $\sim 6.4$  keV), and an obvious cutoff at high energies.

3. The low temperature ( $kT_e \sim 13$  keV) of the hot corona are required in all models. Future X-ray missions (e.g., *Athena*, eXTP, XRISM and HEX-P) may conclusively distinguish between the possible physical scenarios for the coronae.

#### ACKNOWLEDGEMENTS

This work was supported by the National Natural Science Foundation of China (NSFC), Grant No. 11973019, the Natural Science Foundation of Shanghai, Grant No. 22ZR1403400, the Shanghai Municipal Education Commission, Grant No. 2019-01-07-00-07-E00035, and Fudan University, Grant No. JIH1512604. J.J. acknowledges the support from the Leverhulme Trust, the Isaac Newton Trust and St Edmund’s College, University of Cambridge.

#### REFERENCES

- Arnaud, K. A. 1996, in *Astronomical Society of the Pacific Conference Series*, Vol. 101, *Astronomical Data Analysis Software and Systems V*, ed. G. H. Jacoby & J. Barnes, 17
- Axelsson, M., Hjalmarsson, L., & Done, C. 2013, *MNRAS*, 431, 1987, doi: [10.1093/mnras/stt315](https://doi.org/10.1093/mnras/stt315)
- Ballantyne, D. R., McDuffie, J. R., & Rusin, J. S. 2011, *ApJ*, 734, 112, doi: [10.1088/0004-637X/734/2/112](https://doi.org/10.1088/0004-637X/734/2/112)

- Ballantyne, D. R., & Xiang, X. 2020, *MNRAS*, 496, 4255, doi: [10.1093/mnras/staa1866](https://doi.org/10.1093/mnras/staa1866)
- Baloković, M., Harrison, F. A., Madejski, G., et al. 2020, *ApJ*, 905, 41, doi: [10.3847/1538-4357/abc342](https://doi.org/10.3847/1538-4357/abc342)
- Bambi, C., Brenneman, L. W., Dauser, T., et al. 2021, *SSRv*, 217, 65, doi: [10.1007/s11214-021-00841-8](https://doi.org/10.1007/s11214-021-00841-8)
- Baumgartner, W. H., Tueller, J., Markwardt, C. B., et al. 2013, *ApJS*, 207, 19, doi: [10.1088/0067-0049/207/2/19](https://doi.org/10.1088/0067-0049/207/2/19)
- Beloborodov, A. M. 1999a, in *Astronomical Society of the Pacific Conference Series*, Vol. 161, *High Energy Processes in Accreting Black Holes*, ed. J. Poutanen & R. Svensson, 295. <https://arxiv.org/abs/astro-ph/9901108>
- Beloborodov, A. M. 1999b, *ApJL*, 510, L123, doi: [10.1086/311810](https://doi.org/10.1086/311810)
- Bianchi, S., Bonilla, N. F., Guainazzi, M., Matt, G., & Ponti, G. 2009, *A&A*, 501, 915, doi: [10.1051/0004-6361/200911905](https://doi.org/10.1051/0004-6361/200911905)
- Blackman, E. G., & Pessah, M. E. 2009, *ApJL*, 704, L113, doi: [10.1088/0004-637X/704/2/L113](https://doi.org/10.1088/0004-637X/704/2/L113)
- Chartas, G., Rhea, C., Kochanek, C., et al. 2016, *Astronomische Nachrichten*, 337, 356, doi: [10.1002/asna.201612313](https://doi.org/10.1002/asna.201612313)
- Costantini, E., Kriss, G., Kaastra, J. S., et al. 2016, *A&A*, 595, A106, doi: [10.1051/0004-6361/201527956](https://doi.org/10.1051/0004-6361/201527956)
- Crummy, J., Fabian, A. C., Gallo, L., & Ross, R. R. 2006, *MNRAS*, 365, 1067, doi: [10.1111/j.1365-2966.2005.09844.x](https://doi.org/10.1111/j.1365-2966.2005.09844.x)
- Dauser, T., Garcia, J., Wilms, J., et al. 2013, *MNRAS*, 430, 1694, doi: [10.1093/mnras/sts710](https://doi.org/10.1093/mnras/sts710)
- De Marco, B., Ponti, G., Cappi, M., et al. 2013, *MNRAS*, 431, 2441, doi: [10.1093/mnras/stt339](https://doi.org/10.1093/mnras/stt339)
- Dickey, J. M., & Lockman, F. J. 1990, *ARA&A*, 28, 215, doi: [10.1146/annurev.aa.28.090190.001243](https://doi.org/10.1146/annurev.aa.28.090190.001243)
- Done, C., Davis, S. W., Jin, C., Blaes, O., & Ward, M. 2012, *MNRAS*, 420, 1848, doi: [10.1111/j.1365-2966.2011.19779.x](https://doi.org/10.1111/j.1365-2966.2011.19779.x)
- Fabian, A. C., Lohfink, A., Belmont, R., Malzac, J., & Coppi, P. 2017, *MNRAS*, 467, 2566, doi: [10.1093/mnras/stx221](https://doi.org/10.1093/mnras/stx221)
- Fabian, A. C., Lohfink, A., Kara, E., et al. 2015, *MNRAS*, 451, 4375, doi: [10.1093/mnras/stv1218](https://doi.org/10.1093/mnras/stv1218)
- Fabian, A. C., Miniutti, G., Iwasawa, K., & Ross, R. R. 2005, *MNRAS*, 361, 795, doi: [10.1111/j.1365-2966.2005.09148.x](https://doi.org/10.1111/j.1365-2966.2005.09148.x)
- Fabian, A. C., Rees, M. J., Stella, L., & White, N. E. 1989, *MNRAS*, 238, 729, doi: [10.1093/mnras/238.3.729](https://doi.org/10.1093/mnras/238.3.729)
- Fabian, A. C., Zoghbi, A., Ross, R. R., et al. 2009, *Nature*, 459, 540, doi: [10.1038/nature08007](https://doi.org/10.1038/nature08007)
- García, J., Dauser, T., Reynolds, C. S., et al. 2013, *ApJ*, 768, 146, doi: [10.1088/0004-637X/768/2/146](https://doi.org/10.1088/0004-637X/768/2/146)
- García, J., & Kallman, T. R. 2010, *ApJ*, 718, 695, doi: [10.1088/0004-637X/718/2/695](https://doi.org/10.1088/0004-637X/718/2/695)
- García, J., Kallman, T. R., & Mushotzky, R. F. 2011, *ApJ*, 731, 131, doi: [10.1088/0004-637X/731/2/131](https://doi.org/10.1088/0004-637X/731/2/131)
- García, J. A., Fabian, A. C., Kallman, T. R., et al. 2016, *MNRAS*, 462, 751, doi: [10.1093/mnras/stw1696](https://doi.org/10.1093/mnras/stw1696)
- García, J. A., Kallman, T. R., Bautista, M., et al. 2018, in *Astronomical Society of the Pacific Conference Series*, Vol. 515, *Workshop on Astrophysical Opacities*, 282. <https://arxiv.org/abs/1805.00581>
- Ghosh, R., & Laha, S. 2021, *ApJ*, 908, 198, doi: [10.3847/1538-4357/abd40c](https://doi.org/10.3847/1538-4357/abd40c)
- Gierliński, M., & Done, C. 2004a, *MNRAS*, 349, L7, doi: [10.1111/j.1365-2966.2004.07687.x](https://doi.org/10.1111/j.1365-2966.2004.07687.x)
- . 2004b, *MNRAS*, 347, 885, doi: [10.1111/j.1365-2966.2004.07266.x](https://doi.org/10.1111/j.1365-2966.2004.07266.x)
- Gronkiewicz, D., & Różańska, A. 2020, *A&A*, 633, A35, doi: [10.1051/0004-6361/201935033](https://doi.org/10.1051/0004-6361/201935033)
- Guerras, E., Dai, X., Steele, S., et al. 2017, *ApJ*, 836, 206, doi: [10.3847/1538-4357/aa5728](https://doi.org/10.3847/1538-4357/aa5728)
- Guilbert, P. W., Fabian, A. C., & Rees, M. J. 1983, *MNRAS*, 205, 593, doi: [10.1093/mnras/205.3.593](https://doi.org/10.1093/mnras/205.3.593)
- Haardt, F., & Maraschi, L. 1991, *ApJL*, 380, L51, doi: [10.1086/186171](https://doi.org/10.1086/186171)
- Harrison, F. A., Craig, W. W., Christensen, F. E., et al. 2013, *ApJ*, 770, 103, doi: [10.1088/0004-637X/770/2/103](https://doi.org/10.1088/0004-637X/770/2/103)
- Ingram, A., Mastroserio, G., Dauser, T., et al. 2019, *MNRAS*, 488, 324, doi: [10.1093/mnras/stz1720](https://doi.org/10.1093/mnras/stz1720)
- Jansen, F., Lumb, D., Altieri, B., et al. 2001, *A&A*, 365, L1, doi: [10.1051/0004-6361:20000036](https://doi.org/10.1051/0004-6361:20000036)
- Jiang, J., Fabian, A. C., Wang, J., et al. 2019a, *MNRAS*, 484, 1972, doi: [10.1093/mnras/stz095](https://doi.org/10.1093/mnras/stz095)
- Jiang, J., Walton, D. J., Fabian, A. C., & Parker, M. L. 2019b, *MNRAS*, 483, 2958, doi: [10.1093/mnras/sty3228](https://doi.org/10.1093/mnras/sty3228)
- Jiang, J., Parker, M. L., Fabian, A. C., et al. 2018, *MNRAS*, 477, 3711, doi: [10.1093/mnras/sty836](https://doi.org/10.1093/mnras/sty836)
- Jiang, J., Fabian, A. C., Dauser, T., et al. 2019c, *MNRAS*, 489, 3436, doi: [10.1093/mnras/stz2326](https://doi.org/10.1093/mnras/stz2326)
- Kamraj, N., Brightman, M., Harrison, F. A., et al. 2022, *ApJ*, 927, 42, doi: [10.3847/1538-4357/ac45f6](https://doi.org/10.3847/1538-4357/ac45f6)
- Kang, J.-L., & Wang, J.-X. 2022, *ApJ*, 929, 141, doi: [10.3847/1538-4357/ac5d49](https://doi.org/10.3847/1538-4357/ac5d49)
- Kara, E., Alston, W. N., Fabian, A. C., et al. 2016, *MNRAS*, 462, 511, doi: [10.1093/mnras/stw1695](https://doi.org/10.1093/mnras/stw1695)
- Kara, E., García, J. A., Lohfink, A., et al. 2017, *MNRAS*, 468, 3489, doi: [10.1093/mnras/stx792](https://doi.org/10.1093/mnras/stx792)

- Laha, S., Guainazzi, M., Dewangan, G. C., Chakravorty, S., & Kembhavi, A. K. 2014, *MNRAS*, 441, 2613, doi: [10.1093/mnras/stu669](https://doi.org/10.1093/mnras/stu669)
- Ludlam, R. M., Cackett, E. M., Gültekin, K., et al. 2015, *MNRAS*, 447, 2112, doi: [10.1093/mnras/stu2618](https://doi.org/10.1093/mnras/stu2618)
- Lynden-Bell, D. 1969, *Nature*, 223, 690, doi: [10.1038/223690a0](https://doi.org/10.1038/223690a0)
- Madsen, K. K., Harrison, F. A., Markwardt, C. B., et al. 2015a, *ApJS*, 220, 8, doi: [10.1088/0067-0049/220/1/8](https://doi.org/10.1088/0067-0049/220/1/8)
- Madsen, K. K., Fürst, F., Walton, D. J., et al. 2015b, *ApJ*, 812, 14, doi: [10.1088/0004-637X/812/1/14](https://doi.org/10.1088/0004-637X/812/1/14)
- Madsen, K. K., Harrison, F., Broadway, D., et al. 2018, in *Society of Photo-Optical Instrumentation Engineers (SPIE) Conference Series*, Vol. 10699, *Space Telescopes and Instrumentation 2018: Ultraviolet to Gamma Ray*, ed. J.-W. A. den Herder, S. Nikzad, & K. Nakazawa, 106996M, doi: [10.1117/12.2314117](https://doi.org/10.1117/12.2314117)
- Magdziarz, P., Blaes, O. M., Zdziarski, A. A., Johnson, W. N., & Smith, D. A. 1998, *MNRAS*, 301, 179, doi: [10.1046/j.1365-8711.1998.02015.x](https://doi.org/10.1046/j.1365-8711.1998.02015.x)
- Malzac, J., Beloborodov, A. M., & Poutanen, J. 2001, *MNRAS*, 326, 417, doi: [10.1046/j.1365-8711.2001.04450.x](https://doi.org/10.1046/j.1365-8711.2001.04450.x)
- Marinucci, A., Bianchi, S., Braitto, V., et al. 2018, *MNRAS*, 478, 5638, doi: [10.1093/mnras/sty1436](https://doi.org/10.1093/mnras/sty1436)
- McHardy, I. M. 2013, *MNRAS*, 430, L49, doi: [10.1093/mnrasl/sls048](https://doi.org/10.1093/mnrasl/sls048)
- Merloni, A., & Fabian, A. C. 2002, *MNRAS*, 332, 165, doi: [10.1046/j.1365-8711.2002.05288.x](https://doi.org/10.1046/j.1365-8711.2002.05288.x)
- . 2003, *MNRAS*, 342, 951, doi: [10.1046/j.1365-8711.2003.06600.x](https://doi.org/10.1046/j.1365-8711.2003.06600.x)
- Middei, R., Petrucci, P. O., Bianchi, S., et al. 2020, *A&A*, 640, A99, doi: [10.1051/0004-6361/202038112](https://doi.org/10.1051/0004-6361/202038112)
- Mosquera, A. M., Kochanek, C. S., Chen, B., et al. 2013, *ApJ*, 769, 53, doi: [10.1088/0004-637X/769/1/53](https://doi.org/10.1088/0004-637X/769/1/53)
- Nandra, K., & Pounds, K. A. 1994, *MNRAS*, 268, 405, doi: [10.1093/mnras/268.2.405](https://doi.org/10.1093/mnras/268.2.405)
- Nandra, K., Barret, D., Barcons, X., et al. 2013, *arXiv e-prints*, arXiv:1306.2307, doi: [10.48550/arXiv.1306.2307](https://doi.org/10.48550/arXiv.1306.2307)
- Nardini, E., Porquet, D., Reeves, J. N., et al. 2016, *ApJ*, 832, 45, doi: [10.3847/0004-637X/832/1/45](https://doi.org/10.3847/0004-637X/832/1/45)
- Petrucci, P. O., Ursini, F., De Rosa, A., et al. 2018, *A&A*, 611, A59, doi: [10.1051/0004-6361/201731580](https://doi.org/10.1051/0004-6361/201731580)
- Petrucci, P. O., Haardt, F., Maraschi, L., et al. 2001, *ApJ*, 556, 716, doi: [10.1086/321629](https://doi.org/10.1086/321629)
- Petrucci, P. O., Gronkiewicz, D., Rozanska, A., et al. 2020, *A&A*, 634, A85, doi: [10.1051/0004-6361/201937011](https://doi.org/10.1051/0004-6361/201937011)
- Ponti, G., Papadakis, I., Bianchi, S., et al. 2012, *A&A*, 542, A83, doi: [10.1051/0004-6361/201118326](https://doi.org/10.1051/0004-6361/201118326)
- Porquet, D., Reeves, J. N., Matt, G., et al. 2018, *A&A*, 609, A42, doi: [10.1051/0004-6361/201731290](https://doi.org/10.1051/0004-6361/201731290)
- Rees, M. J. 1984, *ARA&A*, 22, 471, doi: [10.1146/annurev.aa.22.090184.002351](https://doi.org/10.1146/annurev.aa.22.090184.002351)
- Reis, R. C., & Miller, J. M. 2013, *ApJL*, 769, L7, doi: [10.1088/2041-8205/769/1/L7](https://doi.org/10.1088/2041-8205/769/1/L7)
- Ricci, C., Trakhtenbrot, B., Koss, M. J., et al. 2017, *ApJS*, 233, 17, doi: [10.3847/1538-4365/aa96ad](https://doi.org/10.3847/1538-4365/aa96ad)
- Ross, R. R., & Fabian, A. C. 1993, *MNRAS*, 261, 74, doi: [10.1093/mnras/261.1.74](https://doi.org/10.1093/mnras/261.1.74)
- . 2005, *MNRAS*, 358, 211, doi: [10.1111/j.1365-2966.2005.08797.x](https://doi.org/10.1111/j.1365-2966.2005.08797.x)
- Shakura, N. I. 1973, *Soviet Ast.*, 16, 756
- Svensson, R. 1984, in *X-ray and UV Emission from Active Galactic Nuclei*, ed. W. Brinkmann & J. Truemper, 152–163
- Svensson, R., & Zdziarski, A. A. 1994, *ApJ*, 436, 599, doi: [10.1086/174934](https://doi.org/10.1086/174934)
- Tashiro, M., Maejima, H., Toda, K., et al. 2018, in *Society of Photo-Optical Instrumentation Engineers (SPIE) Conference Series*, Vol. 10699, *Space Telescopes and Instrumentation 2018: Ultraviolet to Gamma Ray*, ed. J.-W. A. den Herder, S. Nikzad, & K. Nakazawa, 1069922, doi: [10.1117/12.2309455](https://doi.org/10.1117/12.2309455)
- Tazaki, F., Ueda, Y., Ishino, Y., et al. 2010, *ApJ*, 721, 1340, doi: [10.1088/0004-637X/721/2/1340](https://doi.org/10.1088/0004-637X/721/2/1340)
- Tombesi, F., Cappi, M., Reeves, J. N., et al. 2010, *A&A*, 521, A57, doi: [10.1051/0004-6361/200913440](https://doi.org/10.1051/0004-6361/200913440)
- Tortosa, A., Marinucci, A., Matt, G., et al. 2017, *MNRAS*, 466, 4193, doi: [10.1093/mnras/stw3301](https://doi.org/10.1093/mnras/stw3301)
- Tortosa, A., Ricci, C., Tombesi, F., et al. 2022, *MNRAS*, 509, 3599, doi: [10.1093/mnras/stab3152](https://doi.org/10.1093/mnras/stab3152)
- Tsuji, N., Uchiyama, Y., Aharonian, F., et al. 2019, *ApJ*, 877, 96, doi: [10.3847/1538-4357/ab1b29](https://doi.org/10.3847/1538-4357/ab1b29)
- Uttley, P., Cackett, E. M., Fabian, A. C., Kara, E., & Wilkins, D. R. 2014, *A&A Rv*, 22, 72, doi: [10.1007/s00159-014-0072-0](https://doi.org/10.1007/s00159-014-0072-0)
- Vaiana, G. S., & Rosner, R. 1978, *ARA&A*, 16, 393, doi: [10.1146/annurev.aa.16.090178.002141](https://doi.org/10.1146/annurev.aa.16.090178.002141)
- Vasudevan, R. V., & Fabian, A. C. 2007, *MNRAS*, 381, 1235, doi: [10.1111/j.1365-2966.2007.12328.x](https://doi.org/10.1111/j.1365-2966.2007.12328.x)
- Verner, D. A., Ferland, G. J., Korista, K. T., & Yakovlev, D. G. 1996, *ApJ*, 465, 487, doi: [10.1086/177435](https://doi.org/10.1086/177435)
- Walter, R., & Fink, H. H. 1993, *A&A*, 274, 105
- Walton, D. J., Nardini, E., Fabian, A. C., Gallo, L. C., & Reis, R. C. 2013, *MNRAS*, 428, 2901, doi: [10.1093/mnras/sts227](https://doi.org/10.1093/mnras/sts227)
- Walton, D. J., Brightman, M., Risaliti, G., et al. 2018, *MNRAS*, 473, 4377, doi: [10.1093/mnras/stx2659](https://doi.org/10.1093/mnras/stx2659)
- Wik, D. R., Hornstrup, A., Molendi, S., et al. 2014, *ApJ*, 792, 48, doi: [10.1088/0004-637X/792/1/48](https://doi.org/10.1088/0004-637X/792/1/48)

- Willingale, R., Starling, R. L. C., Beardmore, A. P., Tanvir, N. R., & O'Brien, P. T. 2013, *MNRAS*, 431, 394, doi: [10.1093/mnras/stt175](https://doi.org/10.1093/mnras/stt175)
- Winter, L. M., Veilleux, S., McKernan, B., & Kallman, T. R. 2012, *ApJ*, 745, 107, doi: [10.1088/0004-637X/745/2/107](https://doi.org/10.1088/0004-637X/745/2/107)
- Xu, Y., García, J. A., Walton, D. J., et al. 2021, *ApJ*, 913, 13, doi: [10.3847/1538-4357/abf430](https://doi.org/10.3847/1538-4357/abf430)
- Yaqoob, T., Murphy, K. D., Griffiths, R. E., et al. 2007, *PASJ*, 59, 283, doi: [10.1093/pasj/59.sp1.S283](https://doi.org/10.1093/pasj/59.sp1.S283)
- Zdziarski, A. A., Johnson, W. N., & Magdziarz, P. 1996, *MNRAS*, 283, 193, doi: [10.1093/mnras/283.1.193](https://doi.org/10.1093/mnras/283.1.193)
- Zdziarski, A. A., Lightman, A. P., & Maciolek-Niedzwiecki, A. 1993, *ApJL*, 414, L93, doi: [10.1086/187004](https://doi.org/10.1086/187004)
- Zhang, S. N., Feroci, M., Santangelo, A., et al. 2016, in *Society of Photo-Optical Instrumentation Engineers (SPIE) Conference Series*, Vol. 9905, *Space Telescopes and Instrumentation 2016: Ultraviolet to Gamma Ray*, ed. J.-W. A. den Herder, T. Takahashi, & M. Bautz, 99051Q, doi: [10.1117/12.2232034](https://doi.org/10.1117/12.2232034)
- Życki, P. T., Done, C., & Smith, D. A. 1999, *MNRAS*, 309, 561, doi: [10.1046/j.1365-8711.1999.02885.x](https://doi.org/10.1046/j.1365-8711.1999.02885.x)